

Magnetic ground state of monolayer CeI₂: occupation matrix control and DFT+U calculations

Yue-Fei Hou,^{1,2} Shujing Li,³ Xinlong Yang,⁴ Wei Jiang,⁴ Qiu hao Wang,⁴ Fawei Zheng,⁴ Zhen-Guo Fu,^{1,5,*} and Ping Zhang^{1,5,6,†}

¹*Institute of Applied Physics and Computational Mathematics, Beijing 100088, China*

²*Graduate School, China Academy of Engineering Physics, Beijing 100088, China*

³*College of Mathematics and Physics,*

Beijing University of Chemical Technology, Beijing 100029, China

⁴*School of physics, Beijing institute of technology, Beijing 100081, China*

⁵*National Key Laboratory of Computational Physics, Beijing 100088, China*

⁶*School of Physics and Physical Engineering,*

Qufu Normal University, Qufu 273165, China

Abstract

The magnetic ground state is crucial for the applications of the two-dimension magnets as it decides fundamental magnetic properties of the material, such as magnetic order, magnetic transition temperature, and low-energy excitation of the spin waves. However, the simulations for magnetism of local-electron systems are challenging due to the existence of metastable states. In this study, occupation matrix control (OMC) and density functional theory plus Hubbard U calculations are applied to investigate the magnetic ground state of monolayer CeI₂. Following the predicted ferromagnetic (FM) order, the FM ground state and the FM metastable states are identified and found to have different values of the magnetic parameters. Based on the calculated magnetic parameters of the FM ground state, the Curie temperature is estimated to be 128 K for monolayer CeI₂. When spin-orbit coupling (SOC) is considered, the FM ground state is further confirmed to contain both off-plane and in-plane components of magnetization. SOC is shown to be essential for reasonably describing not only magnetic anisotropy but also local electronic orbital state of monolayer CeI₂.

*Corresponding author. Email address: fu_zhenguo@iapcm.ac.cn

†Corresponding author. Email address: zhang_ping@iapcm.ac.cn

I. INTRODUCTION

The two-dimension(2D) magnetsexhibit magnificent potential in spintronic devices and magnetic storage devices due to their unique properties and the nanoscale size. Although Mermin-Wagner theorem [1] denies the possibility of long-range magnetic order in 2D systems at non-zero temperature, a series of experimental studies [2–17] have confirmedthe presence of magnetic orders in 2D materials. These findings encourage people to further explore 2D magnetic materials with superior properties, such as robust dynamic stability, high magnetic transition temperature, and unique magnetic anisotropy.

The magnetic ground state (GS) of a 2D material issignificant. It not only dominates the behaviour about magnetism at low temperature, but decides the low-energy excitation of the spin waves at finite temperature. For magnetic crystals, a comprehensive description of the magnetic GS should contain the information of two aspects: the specific magnetic structure and the electronic states of the magnetic sites. For the former part, Spin-polarized scanning tunneling microscope (SP-STM), Ramam spectroscopy, and the observation of anomalous Hall effect have been adopted to examine the magnetic order of 2D magnetic insulators and 2D magnetic metals [3, 12, 17–20]. For the latter part, x-ray magnetic circular dichroism (XMCD) and x-ray magnetic linear dichroism(XMLD) are two techniques which help to obtain the local electronic configuration [21, 22]. Nonetheless, exploring magnetic ground states of 2D materials experimentally is still challenging. The limitations include the acquirement of high quality samples, strict experimental conditions, and even expensive costs on economy and time. From this point of view, exploring 2D magnetic materials by using density functional theory (DFT) calculations is another feasible scheme. The DFT tool gives the prediction of the magnetic ground state without synthesizing actual samples. It has been applied to study a series of 2D magnetic materials such as layered α - RuCl_3 , $\text{VSe}(\text{Te})_2$, $\text{CrGe}(\text{Si})\text{Te}_3$, etc. [23–33] For 2D CrI_3 and CrBr_3 , DFT calculations give quite consistent prediction of magnetic features with the experiments, including the magnetic structure and Curie temperature (T_C) [34–37]. With the assistance of DFT calculations, the studying progress of 2D magnetic materials has been accelerated significantly.

In 2D magnetic insulators and semiconductors, the spin moments are commonly contributed by polarized electrons from partially filled d or f atomic shells. These electrons are localized around the lattice sites and need extra corrections for strong electronic correla-

tion. Therefore, the density functional theory plus Hubbard U (DFT+U) scheme [38, 39] is widely applied to give reasonable electronic structures of the correlated systems. In fact, the conventional DFT+U computational scheme faces challenges in locating the ground state of the localized electrons due to the presence of metastable states, especially when the d and f shells are less filled. In other words, although a specific magnetic ordered state can be determined by DFT+U calculations, however, the obtained electronic state of the localized electrons may be not identical for different researchers. This phenomenon has appeared in the DFT+U studies of Ti-based systems [40], Ce-based systems [40, 41], U-based systems [42–47], cubic fluorite PuO_2 [48, 49], etc., and the metastable states can originate from $3d$, $4f$, or $5f$ localized electrons (not found in $4d$ or $5d$ electronic systems yet, to our knowledge). Moreover, these works have also shown that the occurrence of trapping into metastable states is not relevant to the form of adopted exchange-correlation functional. Local density approximation (LDA) [41], generalized gradient approximation (GGA) [40, 42–44], strongly constrained appropriate normed (SCAN) type meta-GGA [49], and HSE06 type hybrid [50, 51] functionals have been adopted in the studies but this accident still happens constantly. To solve the problem, a few techniques have been developed including U-ramping [47, 52], quasi-annealing [53], occupation matrix control (OMC) [40, 43, 47, 54–56], DFT+DMFT [57] and even the combination of them [58]. These techniques help to reduce the probability of trapping into metastable states to some extent. However, it remains an open question as to how the ground state of the localized electrons can be accurately obtained.

Recently, the monolayer CeI_2 was predicted to be an in-plane ferrimagnetic (FM) semiconductor with a high T_C of 374 K by DFT+U calculations [59]. The dynamic stability of the monolayer CeI_2 was supported by both phonon calculations and a molecular dynamics simulation at room temperature. In the monolayer CeI_2 , two $6s$ electrons of the Ce atom move away to form the Ce-I bond, leaving a $4f^1 5d^1$ electronic configuration for the Ce^{2+} ion. According to above analysis, a number of metastable states originated from the highly localized $4f$ electrons should be expected. Owing to the importance for both basic physics and potential applications, it is necessary to provide a systematic analysis of the magnetic GS of monolayer CeI_2 .

In this study, we perform DFT+U calculations combined with OMC to investigate the magnetic GS of monolayer CeI_2 . The magnetic structure is once again confirmed to be FM. The FM GS as well as twenty-three FM metastable states of monolayer CeI_2 with different

local electronic states are identified. Our results show that the calculated isotropy exchange parameter and magnetic anisotropy energy are distinguishable for the GS and metastable states. Based on the exchange parameters of the magnetic GS, the T_C is estimated to be about 128 K by using Monte Carlo simulations. To reasonably analyze the contributions to the total energies, the Coulomb potential energies of the $4f$ electron with different occupied electronic orbitals in the crystal field are discussed. Furthermore, we take spin-orbit coupling (SOC) into consideration. The magnetic structure of monolayer CeI_2 then becomes FM with both in-plane and off-plane components of magnetic moments and the easy axis of magnetization is coupled with the crystal structure. The single Ce- $4f$ electron occupies another distinguishable electronic orbital compared to the situation without SOC, which illustrates that SOC is essential to describe the magnetic GS of monolayer CeI_2 . A fully off-plane FM state is confirmed to be a metastable state of monolayer CeI_2 whose total energy is just slightly higher than the magnetic GS. We anticipate that achieving saturation magnetization in the off-plane direction for monolayer CeI_2 is feasible under appropriate external conditions.

II. COMPUTATIONAL METHODS

The DFT+U calculations are carried out by employing the Vienna abinitiosimulation package (VASP) code [60]. OMC is implemented by applying the patch of Allen *et al.* tailored for VASP [40]. The adopted atomic pseudo potentials are constructed by the project augmented wave (PAW) method [61–63]. The cut-off energy of the plane wave bases is set to 600 eV. The first Brillouin Zone is sampled by a Γ -center $11 \times 11 \times 1$ k -point mesh. The convergence of both cut-off energy and k -point mesh has been carefully examined. The crystal structures are relaxed until the Feynman-Hellman force on each atom is smaller than 0.005 eV/Å. The optimizing of the charge density is ended when the energy difference is smaller than 10^{-6} eV between the current two steps of the iteration. We make use of the DFT+U method of Dudarev *et al.* [39] with a form of

$$E_{\text{DFT+U}} = E_{\text{DFT}} + \frac{U - J}{2} \sum_{\sigma} \left[\left(\sum_{m_1} n_{m_1, m_1}^{\sigma} \right) - \left(\sum_{m_1, m_2} n_{m_1, m_2}^{\sigma} n_{m_2, m_1}^{\sigma} \right) \right], \quad (1)$$

where n_{m_1, m_2}^{σ} is the matrix element of the occupation matrix with spin σ . The standard DFT part here is handled by the Perdew-Burke-Ernzerhof (PBE) type GGA exchange-correlation

functional [64] The Hubbard U and Hund J for the Ce- $4f$ electron are set to be 7.47 eV and 0.99 eV, respectively, which have been applied in previous study [59, 65]. To be cautious, a discussion is also made to demonstrate the rationality of the U parameter (see Section B of the Supporting information). Based on the calculated Bloch states by plane waves bases, Wannier90 code [66] is used to construct the tight-binding Hamiltonian. TB2J code [67] is used to calculate the Green's function and then the isotropic exchange parameter for magnetic properties is obtained. The T_C is gained by Monte Carlo simulations based on the heat bath algorithms [68]. The visualizations of the crystal structure and spin densities in this work is achieved by VESTA [69]. The VASPKIT code is used to process the data of the DFT calculations [70].

III. OMC OF THE $4f^1$ ELECTRONIC STATE

A quantum state of a single electron can be express as a linear combination of a group of complete and orthogonal bases in the Hilbert space. In the limitation of localized electrons of an isolated atom, the dimension of the space is equal to $2l+1$, where l is the angular quantum number of that electron. In monolayer CeI₂, l is no longer a good quantum number for the $5d$ electron of Ce²⁺ since the $5d$ electron is not well localized. Additionally, the delocalized $5d$ electron has a more plane-wave-like charge density rather than the atomic-orbital-like charge density of the $4f$ electron. Hence only the $4f$ electron is accompanied by high risks of falling into metastable states in DFT+U calculations. Its electronic orbital requires careful control and observation.

The occupation matrix is the density matrix in particle-number representation and a 14×14 occupation matrix is sufficient to represent the electronic state of the single $4f$ electron exactly. Here the general set of $4f$ atomic orbitals is used as the bases, which are $f_{y(3x^2-y^2)\uparrow}$, $f_{xyz\uparrow}$, $f_{yz^2\uparrow}$, $f_{z^3\uparrow}$, $f_{xz^2\uparrow}$, $f_{z(x^2-y^2)\uparrow}$, $f_{x(x^2-3y^2)\uparrow}$, $f_{y(3x^2-y^2)\downarrow}$, $f_{xyz\downarrow}$, $f_{yz^2\downarrow}$, $f_{z^3\downarrow}$, $f_{xz^2\downarrow}$, $f_{z(x^2-y^2)\downarrow}$, and $f_{x(x^2-3y^2)\downarrow}$, respectively. The spin-quantization axis is chosen to be along z direction of the Cartesian coordinate system. We firstly do not take SOC into consideration. Since there is only one localized electron in the $4f$ shell of Ce²⁺, any quantum state of the single electron with both spin up and spin down components is unphysical. We thus neglect the spin index and a quantum state of the single $4f$ electron can be written as

$$\psi_{4f} = c_1 f_{y(3x^2-y^2)} + c_2 f_{xyz} + c_3 f_{yz^2} + c_4 f_{z^2} + c_5 f_{xz^2} + c_6 f_{z(x^2-y^2)} + c_7 f_{x(x^2-3y^2)}, \quad (2)$$

where c_i ($i = 1, 2, \dots, 7$) is the complex expansion coefficient of the basis. There should be

$$\sum_i c_i = 1. \quad (3)$$

For simplicity, we mark the quantum state as $(c_1, c_2, c_3, c_4, c_5, c_6, c_7)$ for the following part of this paper. The eigenvectors and eigenvalues of the occupation matrix are actually quantum states and the corresponding occupation numbers, respectively.

An OMC procedure is to set a initial occupation matrix artificially for the localized electrons in the DFT+U calculations. The initial occupation matrix has also been called the starting point [56]. Different starting points may access to different final states of the localized electrons. In our calculations, we make our starting points for the Ce-4*f* electron all diagonal with a average occupation on several orbital bases. The down spin block and the two off-diagonal blocks of the 14×14 occupation matrix are null matrices. The up spin block of the occupation matrix has a form of

$$\begin{pmatrix} a_1 & 0 & \cdots & 0 \\ 0 & a_2 & \cdots & 0 \\ \cdots & \cdots & \cdots & \cdots \\ 0 & 0 & \cdots & a_7 \end{pmatrix} \quad (4)$$

with

$$a_i = 0, \text{ or } \frac{1}{n} \quad (i, n = 1, 2, \dots, 7), \quad (5)$$

where n is the number of orbital bases whose occupation number is non-zero. The trace of the up spin block is the number of occupying electrons, which is equal to 1 for the Ce-4*f* shell here. Hence there is

$$\sum_i a_i = 1. \quad (6)$$

Based on Eqs. (4)-(6), we have $\sum_{i=1}^7 C_7^i = 127$ different starting points for the DFT+U calculations. After the self-consistence iteration processes based on different starting points, we obtain twenty-four final states of monolayer CeI₂, whose 4*f* electronic states are different with each other. A detailed discussion of the OMC procedure for the SOC situation is provided in Section C of the Supporting information.

IV. MAGNETIC PROPERTIES OF THE GS AND METASTABLE STATES

The optimized crystal structure of monolayer CeI₂ is shown in Fig. 1(a). Each Ce²⁺ ion is surrounded by six nearest I⁻ ions which form a regular triangle prism (RTP). The distance between two nearest Ce²⁺ ions is 4.28 Å which makes the direct exchange from different Ce sites negligible. The main reason that causes the magnetic order should be the superexchange interaction mediated by I-*p* electrons. Since both Ce-4*f* and Ce-5*d* electrons contribute to the superexchange interaction, the total inter-site exchange strength can be decomposed to J^{d-d} , J^{d-f} , and J^{f-f} , as shown in Fig. 1(b). These are the exchange parameter between 5*d* shell and 5*d* shell, 5*d* shell and 4*f* shell, and 4*f* shell and 4*f* shell from different sites, respectively. Meanwhile, with the help of coordinated I⁻ ions, the *d* – *f* hybridization on each Ce site should be considered. This on-site *d* – *f* exchange parameter is denoted by J^{site} , as shown in Fig. 1(b). For the inter-site exchange parameters, we only consider the first nearest exchange parameter J_1 and second nearest exchange parameter J_2 as shown in Fig. 1(a). Hence the total Hamiltonian of CeI₂ can be express as

$$\hat{H}_{\text{tot}} = \delta - J_1 \sum_{\langle i,j \rangle} \vec{S}_i \cdot \vec{S}_j - J_2 \sum_{\langle\langle i,j \rangle\rangle} \vec{S}_i \cdot \vec{S}_j - J^{\text{site}} \sum_i \vec{S}_i^d \cdot \vec{S}_i^f \quad (7)$$

with

$$J_1 = J^{d-d} + J^{d-f} + J^{f-f}, \quad (8)$$

where δ is the spin-independent part of the total energy. i and j denote different sites in the unit cell.

All the following discussions for monolayer CeI₂ are based on the fact that the magnetic structure of the GS is FM no matter which orbital the localized electron is occupying. This feature of CeI₂ has been verified by our calculations for the total energy and exchange parameters as introduced in the following section. With OMC applied, the relative energies of the GS and the metastable states of FM CeI₂ are listed in Table I. It is noteworthy that the FM state studied by the former study [59] is confirmed to be a metastable state (S₂₀) in our work.

By using a model Hamiltonian of spin interactions like Eq. (7) in combination with the DFT total energies of different magnetic structures, one can fit the values of the exchange parameters. However, this scheme is invalid for monolayer CeI₂ because the exchange parameter is not identical for different magnetic structures. A detailed discussion about it is

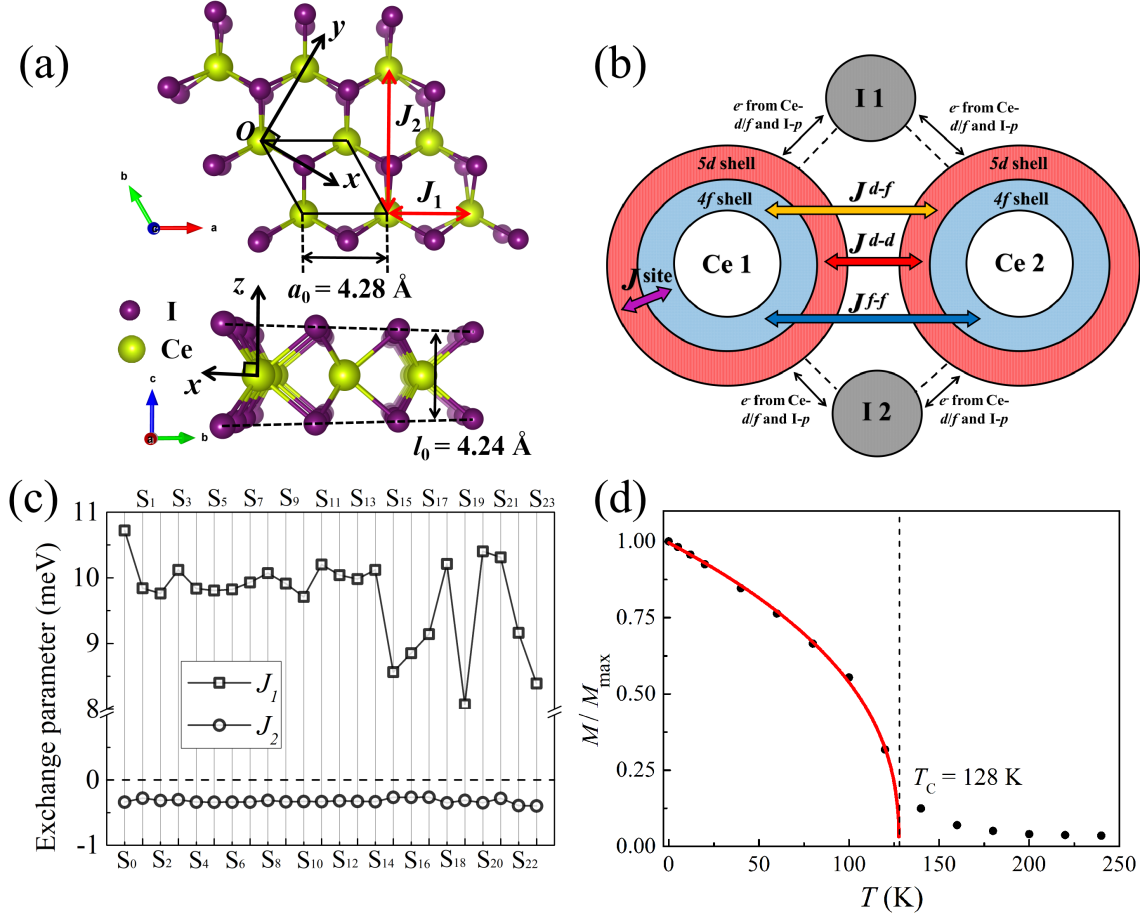


FIG. 1: (Color online) (a) The optimized crystal structure of monolayer CeI₂. a_0 and l_0 are the lattice parameter and thickness of monolayer CeI₂. (b) The components (J^{d-d} , J^{d-f} , and J^{f-f}) of the first nearest inter-site exchange parameter and the on-site $d-f$ exchange parameter (J^{site}) in monolayer CeI₂. (c) The values of first nearest exchange parameter J_1 and second nearest exchange parameter J_2 for the GS and metastable states. (d) The temperature dependent magnetization intensity of monolayer CeI₂ with a quenching at 128 K predicted by Monte-Carlo simulations.

given in Section D of the Supporting information. Here, we make use of the obtained Bloch states by a self-consistence calculation to construct tight-binding Hamiltonian and calculate the exchange parameter by using Green's function method [67]. The values of J_1 and J_2 for monolayer CeI₂ with different local electronic states are shown in Fig. 1(c). One can find that J_1 is always positive and J_2 is always negative for all the states. The absolute value of J_1 is far greater than J_2 , which favors FM order of monolayer CeI₂. Note that J_1 is quite

sensitive to the $4f$ electronic states.

The exchange parameters of the ground state S_0 are used to simulate the T_C of monolayer CeI_2 . There are $J_1 = 10.7$ meV and $J_2 = -0.34$ meV. Monte-Carlo method is used and T_C is estimated to be about 128 K as shown in Fig. 1(d). It is important to note that the presence of metastable states of monolayer CeI_2 can lead to different values of the inter-site exchange parameters, potentially affecting the reliability of the predicted T_C for the material. Therefore, it is also recommended to exclude the metastable states before conducting further calculations for other local-electron systems, in addition to monolayer CeI_2 .

In the case of weak SOC (common in $3d$ electronic systems), the orbital state of localized electrons is primarily decided by on-site Coulomb interactions and the crystal field. Thus, SOC can be treat as an additional perturbation. In other words, the SOC energy can be safely gained based on the simulated charge density which does not include SOC effect. The SOC Hamiltonian is written as

$$H_{\text{SOC}} = -\lambda \vec{L} \cdot \vec{S}, \quad (9)$$

where λ parameter denotes the strength of SOC. Applying this approximation to FM monolayer CeI_2 , the relative energies of different spin directions are calculated. As shown in Table I, all the states have the highest energy when the spin is along z direction. The easy axis of spin polarization varies depending on the specific orbital state of the $4f$ electron. For S_0 (the GS), both x and y directions are the easy axes which are $390 \mu\text{eV}$ lower in energy than the z direction. Hence, monolayer CeI_2 is recognized as an isotropic in-plane FM material within the theoretical framework of weak SOC.

In order to better understand the origin of the FM order in monolayer CeI_2 , the components of J_1 are calculated and listed in Table I. It is observed that the values of J^{d-d} , J^{d-f} , and J^{f-f} are always in the order of $J^{d-d} > J^{d-f} > J^{f-f}$ for different states. J_1 is primarily contributed by J^{d-d} , which is similar to the situation in GdI_2 ($Gd^{2+}: 4f^7 5d^1$) [71]. According to Eq. (7), J^{site} can be obtained from the energy difference of two spin configurations: $4f^\uparrow 5d^\uparrow$ and $4f^\uparrow 5d^\downarrow$ for each state, i.e. $J^{\text{site}} = 1/2 (E_{\text{tot}}^{\uparrow\uparrow} - E_{\text{tot}}^{\downarrow\downarrow})$. The calculated values of J^{site} for different states are listed in Table I. The positive value of J^{site} helps to stabilize the saturated spin moment of Ce^{2+} , i.e. $4f^\uparrow 5d^\uparrow$ spin configuration is favorable in energy for monolayer CeI_2 rather than $4f^\uparrow 5d^\downarrow$ spin configuration, although the spin singlet state ($^1G_0^4$) has been recommended by laser spectroscopy for Ce atoms [72]. Note that S_0 has the largest value of J^{site} , which is one of the reason why it leads to the lowest total energy

TABLE I: The 1st column lists the GS (S_0) and the metastable states (S_1 - S_{23}). The 2nd column gives the DFT total energies of all the FM states relative to the GS denoted as ΔE (in unit of meV). The 3rd column shows the specific representations of the calculated $4f^1$ states with $f_{y(3x^2-y^2)}$, f_{xyz} , f_{yz^2} , f_{z^3} , f_{xz^2} , $f_{z(x^2-y^2)}$, and $f_{x(x^2-3y^2)}$ as bases. The 4th to the 6th columns give the relative energies of x , y , and z directions of spin polarization for each state (in unit of μeV). The 7th to the 10th columns give the values of J^{site} , J^{d-d} , J^{d-f} , and J^{f-f} for each state (in unit of meV).

	ΔE	$4f^1$ electronic state	x	y	z	J^{site}	J^{d-d}	J^{d-f}	J^{f-f}
S_0	0	(0.66, 0, 0, -0.74, 0, 0, 0)	0	0	393	116.1	10.2	0.30	0.22
S_1	4.4	(0, 0, 0, -0.74, 0, 0, 0.66)	0	0	381	113.9	9.18	0.38	0.28
S_2	5.0	(0.62, 0, 0.4, 0.6, 0, -0.3, 0)	0	0	409	104.3	9.10	0.49	0.17
S_3	5.0	(0.38, 0.1, 0.33, -0.61, 0.29, 0, -0.53)	0	6	406	107.4	8.60	1.42	0.10
S_4	6.6	(0.62, 0, -0.79, 0, 0, 0, 0)	0	24	461	97.3	9.04	0.56	0.24
S_5	6.6	(0.61, 0, 0.38, 0, -0.69, 0, 0)	9	0	455	97.3	9.58	0.20	0.03
S_6	7.3	(0.54, 0, 0.28, 0, 0.73, 0, 0.29)	27	0	460	96.9	9.22	0.40	0.21
S_7	7.6	(0.5, 0, -0.77, 0, 0.16, 0, -0.34)	0	25	458	96.7	9.33	0.50	0.10
S_8	7.6	(0.24, 0.1, 0.5, -0.45, 0.37, 0, -0.58)	0	13	425	101.6	8.78	1.14	0.15
S_9	8.3	(0.43, 0, -0.76, 0, 0.2, 0, -0.43)	0	25	456	96.3	9.22	0.70	0.01
S_{10}	8.4	(0.42, 0, 0.19, 0, -0.76, 0, -0.45)	17	0	462	96.2	8.34	1.24	0.13
S_{11}	8.5	(0.4, 0, 0.57, 0, 0.54, 0, -0.47)	0	12	449	96.2	8.70	1.32	0.18
S_{12}	9.9	(0, 0, 0, 0, 0.79, 0, 0.61)	46	0	460	95.4	8.86	0.67	0.51
S_{13}	9.9	(0, 0, -0.68, 0, -0.4, 0, 0.61)	0	23	450	95.4	9.16	0.60	0.22
S_{14}	24.1	(0.33, 0, 0.6, 0, -0.52, 0, 0.52)	0	15	449	80.8	8.25	1.49	0.38
S_{15}	33.3	(0, 1, 0, 0, 0, 0, 0)	44	0	428	49.0	7.83	0.50	0.24
S_{16}	33.3	(0, 0, 0, 0, 0, 1, 0)	0	43	427	49.0	7.99	0.60	0.26
S_{17}	33.3	(0, -0.92, 0, 0, 0, 0.4, 0)	29	0	421	49.0	7.14	1.38	0.62
S_{18}	188.9	(0.8, 0, 0.6, 0, 0, 0, 0)	0	144	363	103.2	9.50	0.46	0.25
S_{19}	190.1	(0, 0, 0, -1, 0, 0, 0)	0	0	619	109.9	6.86	1.19	0.02
S_{20}	276.5	(1, 0, 0, 0, 0, 0, 0)	0	0	101	114.8	9.92	0.38	0.10
S_{21}	276.0	(0, 0, 0, 0, 0, 0, 1)	0	0	75	111.3	10.0	0.34	-0.03
S_{22}	279.2	(0.25, 0, 0.97, 0, 0, 0, 0)	0	183	698	89.8	7.73	1.40	0.03
S_{23}	280.2	(0, 0, 0, 0, 0.97, 0, -0.25)	175	0	692	88.5	6.89	1.14	0.36

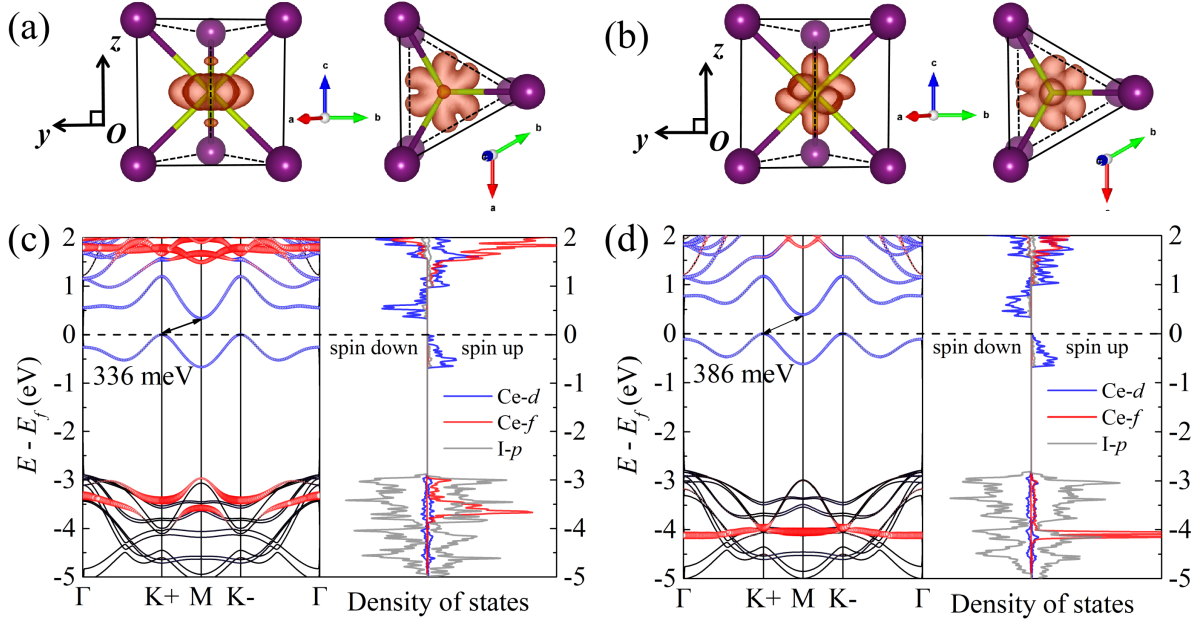


FIG. 2: (Color online) The isosurfaces of spin densities for (a): S_{20} and (b): S_0 . The energy bands and density of states of (c): S_{20} and (d): S_0 . The contributions of Ce- d and Ce- f orbitals to the bands are represented by the blue and red bubbles, respectively.

referring to Eq. (7).

The spin densities and electronic structures of S_{20} and S_0 are illustrated in Fig. 2. The significant difference between the two states can be noticed by inspecting the spin densities. Meanwhile, S_0 exhibits more low-energy contributions to the bands from $4f$ orbitals than that of S_{20} . The $E - k$ dispersion of the $4f$ electron is much more weak for S_0 , almost forming a flat band at -4.1 eV. Since there is $d - f$ hybridization on each Ce site mediated by I^- ions, the $5d$ electronic states are slightly affected by the $4f$ electronic states as well. The energy gaps of S_0 and S_{20} , which are caused by the spin splitting of the $5d$ electrons, are 386 meV and 336 meV, respectively. The spin densities and electronic structures of all the other states are also shown in Section F of the Supporting information.

V. ELECTRONIC ORBITAL ENERGY IN THE RTP CRYSTAL FIELD

In order to have a better understanding of the ground state of FM monolayer CeI_2 , we calculate the electronic orbital energies of the single $4f$ electron occupying different orbitals

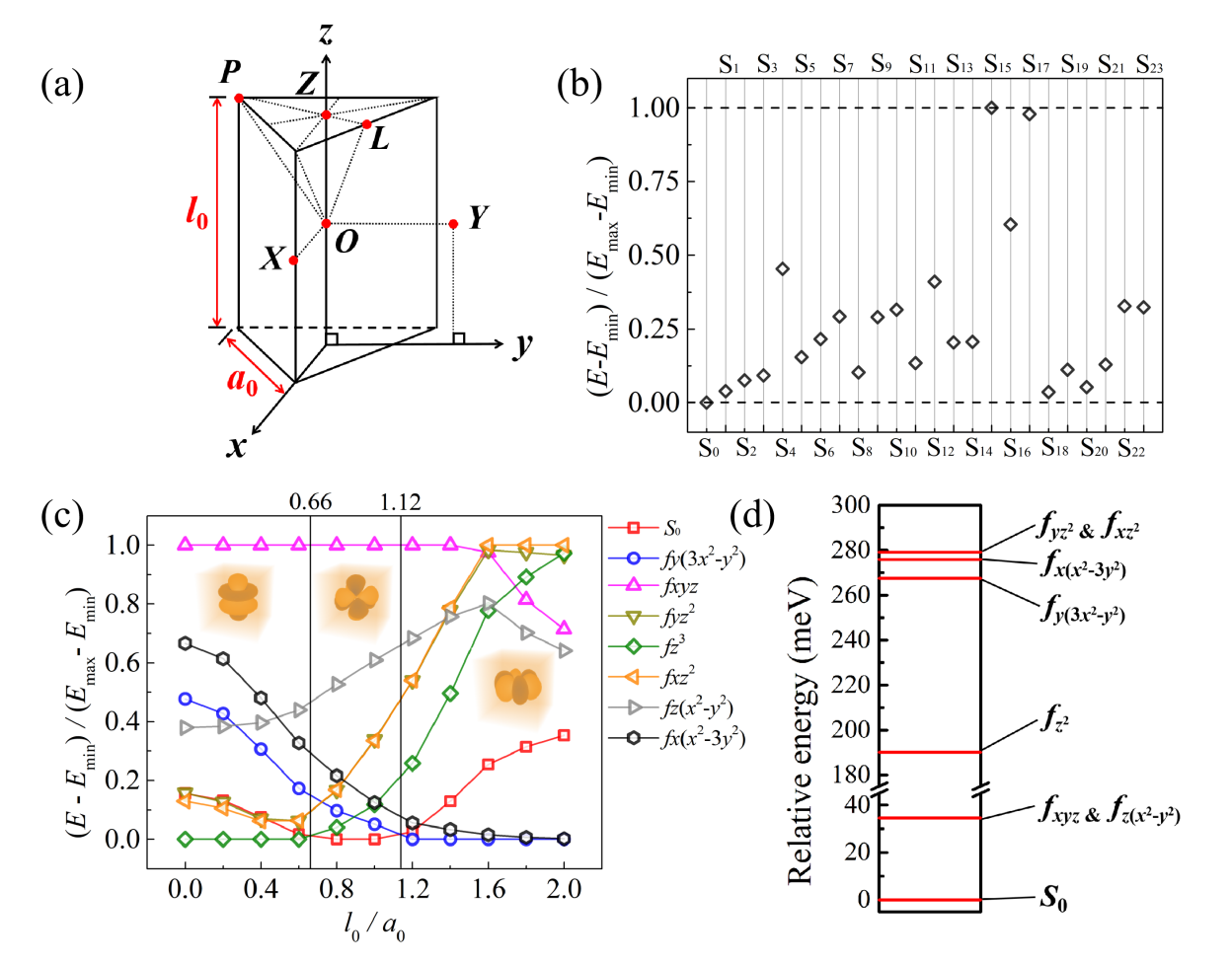


FIG. 3: (Color online) (a) The RTP crystal field model in monolayer CeI_2 with the first nearest I^- ions being considered only. (b) The relative 4f electronic orbital energies in the RTP crystal field of the 24 identified FM states. The lowest orbital energy is set to 0. (c) The relative crystal field orbital energies of several 4f electronic orbitals with variable shape of the RTP. Here S_0 represents the single electronic orbital: $0.66f_{y(3x^2-y^2)} - 0.74f_{z^3}$. For the three ranges of l_0/a_0 , the corresponding electronic orbital with the lowest energy is visualized. The rest of these orbitals are visualized in Section A of the Supporting information. (d) The relative DFT total energies of monolayer CeI_2 with the 4f electron occupying different orbitals which are discussed in (c).

in RTP crystal field. This so-called orbital energy is originated from pure Coulomb interactions. As shown in Fig. 3(a), the single 4f electron is located at O , with six surrounding anions located at R_i (x_i, y_i, z_i) ($i = 1, 2, \dots, 6$) in the Cartesian coordinate system. The height of the RTP is denoted as l_0 and the edge length of the bottom surface is denoted as

a_0 . l_0 and a_0 are taken to be 4.24 Å and 4.28 Å, respectively, which are based on the relaxed monolayer CeI₂ by DFT calculations. The orbital energy can be expressed as

$$\langle E_{4f} \rangle = \langle \psi_{4f} | V_{\text{CF}} | \psi_{4f} \rangle, \quad (10)$$

where ψ_{4f} is the wave function of the single $4f$ electron and V_{CF} is the crystal field potential energy with a form of

$$V_{\text{CF}} = \sum_{i=1}^6 \frac{1}{\sqrt{(x-x_i)^2 + (y-y_i)^2 + (z-z_i)^2}}, \quad (11)$$

in which the constant term has been set to be unity for simplicity in the calculations. The charge densities of the six I⁻ ions are treated as point charges. The orbital energies of all the identified $4f^1$ electronic states listed in Table I are calculated. As shown in Fig. 3(b), the $4f$ electronic state for S₀ has the lowest orbital energy in the RTP crystal field. Now we can see that besides the largest value of J^{site} , the RTP crystal field in monolayer CeI₂ also helps to stabilize the ground state S₀ by attaching the lowest $4f$ electronic orbital energy.

We explore how the orbital energies are influenced by the shape of the RTP. The $4f$ electronic orbital of S₀ and the seven general $4f$ atomic orbitals are examined, as shown in Fig. 3(c). Keeping a_0 unchanged and l_0/a_0 can be taken as the unique variable. For $0 < l_0/a_0 < 0.66$, f_{z^3} has the lowest orbital energy. Especially when l_0/a_0 is equal to 0, the crystal field is a 2D regular triangle crystal field. For $0.66 < l_0/a_0 < 1.12$, i.e. the RTP becomes taller, the $4f$ orbital state of S₀ has the lowest orbital energy. Note that l_0/a_0 is equal to 0.99 when no strain is imposed to monolayer CeI₂. For $l_0/a_0 > 1.12$, $f_{y(3x^2-y^2)}$ has the lowest orbital energy. Now we can conclude that an appropriate shape of the RTP crystal field is indeed necessary for S₀ to maintain its lowest $4f$ electronic orbital energy. In fact, l_0/a_0 can only vary in a small range in monolayer CeI₂. The value of l_0/a_0 varies from 0.83 (for 10% tensile strain) to 1.08 (for 5% compressive strain) according to our simulations. This implies the lowest $4f$ electronic orbital energy for S₀ is robust in monolayer CeI₂ even if some external forces are imposed.

Since OMC is applied, the DFT total energy of the system with the $4f$ electron occupying arbitrary orbital is able to be gained as long as that $4f$ electronic state is metastable. Due to the high symmetry of the crystal field in monolayer CeI₂, the seven general $4f$ atomic orbitals are all metastable to be occupied individually. The corresponding DFT total energies are

excerpted from Table I and shown in Fig. 3(d). The FM states of CeI₂ with the 4*f* electron occupying f_{xz^2} and f_{yz^2} , respectively, are nearly degenerate and they also have equal orbital energy for the 4*f* electron referring to Fig. 3(c). However, the two states with the 4*f* electron occupying f_{xyz} and $f_{z(x^2-y^2)}$, respectively, are degenerate but with unequal orbital energies for the 4*f* electron. Since these two states also have the same value of J^{site} (refer to Table I, S₁₅ and S₁₆), there should be extra factors that balance the energy difference caused by the 4*f* orbital energies. This reminds us the corresponding 5*d* electronic states should also be responsible for the total energies. A detailed discussion about this part is given in Section E of the Supporting information. In short, a complete understanding of the ground state of monolayer CeI₂ requires both 4*f* and 5*d* electronic characters although OMC is only necessary for 4*f* electrons in the DFT+U calculations.

VI. THE MAGNETIC GS WITH STRONG SOC

In the more realistic situation, the electronic state of the localized 4*f* electron in monolayer CeI₂ is not only decided by electronic interactions, but also decided by strong SOC. Thus, the acquirement of the magnetic GS requires fully unconstrained noncollinear self-consistence calculations [72] with SOC included in the DFT+U energy functional. Here OMC is once again applied to exclude metastable states. With SOC being considered, the magnetic ground state of monolayer CeI₂ still favors FM order but the magnetic moments are with components of both *y* and *z* directions, as shown in Fig. 4(a). The easy axis of magnetization is coupled with the crystal field, which makes the magnetic moments point toward certain directions of the crystal structure. The ratio of the off-plane (*z*) and in-plane (*y*) components of the total magnetic moment is 0.65 : 1. The net magnetic moment for each Ce is about 1.92 μB .

Although the crystal structure of monolayer CeI₂ is only triply rotationally invariant, the magnetic GS is recommended to be six-fold degenerate by our DFT calculations. Here it is assumed that there is no difference between *z* and $-z$ directions. As displayed in Fig. 4(b), the magnetization density of magnetic GS is chiral. For two directions of magnetization marked by either two “+” or two “-”, the magnetization densities overlap completely with each other after a $\pm 2/3\pi$ rotation along *z*-axis, which are with the same chirality. For two directions of magnetization marked by “+” and “-”, respectively, the magnetization

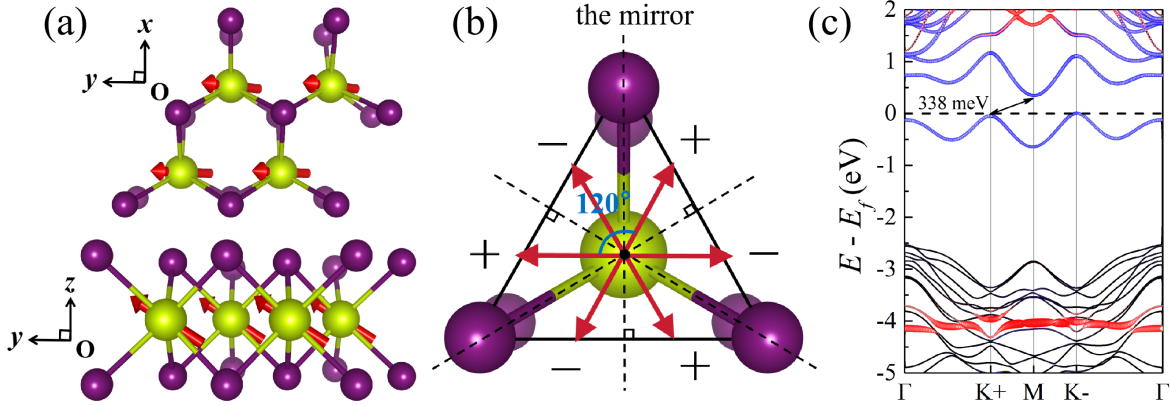


FIG. 4: (Color online) (a) The FM structure of the GS of monolayer CeI_2 with SOC included. The component of x direction for the magnetic moment is strictly equal to 0. (b) The six-fold symmetry of the magnetic GS of monolayer CeI_2 with SOC included. The red arrows only represent the in-plane component of the magnetic moments. (c) The SOC energy bands of the GS of monolayer CeI_2 . The contributions of Ce-d and Ce-f orbitals to the bands are represented by the blue and red bubbles, respectively.

densities overlap completely with each other after a mirror-like inversion by the “ $x - z$ ” type plane, which are with opposite chirality. As all these six magnetization densities have the equal and lowest total energy, we expect this six-fold symmetry of magnetization could be verified by the measurements of magnetic susceptibility experimentally. The SOC bands of monolayer CeI_2 is shown in Fig. 4(c). No significant and qualitative changes are detected for the electronic structure near the fermi level when compared with the situation without SOC. In spite of this, SOC is essential to reasonably describe the magnetic anisotropy in monolayer CeI_2 .

When searching for the magnetic GS of monolayer CeI_2 with SOC, a fully off-plane FM metastable state is confirmed. A comparison between this metastable state and the GS is shown in Table II. The included angle of the magnetic moments from the two FM states is 57° . The fully off-plane FM state is 0.94 meV per unit cell higher in total energy than the FM GS. This energy difference is obtained with the Jahn-Teller distortion of the crystal structure being considered in the simulation. If the Jahn-Teller distortion is removed, the energy

TABLE II: The comparison between the FM GS (G_{FM}^0) and the fully off-plane FM metastable state (G_{FM}^z) of monolayer CeI₂ with SOC included. The 2nd column shows the magnetic moment vectors \vec{S} of the two states. The 3rd column shows the relative energies of the two states ΔE (in unit of meV). The 4th and 5th columns are the lattice parameters a_0 and thicknesses l_0 of monolayer CeI₂ with Jahn-Teller distortions being imposed. The 6th column shows the specific representation of the $4f^1$ electronic states with $f_{y(3x^2-y^2)}$, f_{xyz} , f_{yz^2} , f_{z^3} , f_{xz^2} , $f_{z(x^2-y^2)}$, and $f_{x(x^2-3y^2)}$ as bases. \uparrow and \downarrow denote the status of spin.

	\vec{S}	ΔE (meV)	a_0 (Å)	l_0 (Å)	$4f^1$ electronic states
G_{FM}^z	(0, 0, 1)	0.94	4.28	4.23	$(0.61, 0, 0, -0.72, 0, 0, 0.267i)^\uparrow$ $+(0, 0, -0.11i, 0, -0.11, 0, 0)^\downarrow$
G_{FM}^0	(0, 0.84, 0.55)	0	4.29	4.22	$(0.57, 0, -0.15i, 0.6, 0, 0, 0.19i)^\uparrow$ $+(-0.23 + 0.15i, 0, 0.14i, -0.3 + 0.18i, 0.1, 0, 0)^\downarrow$

difference becomes 0.72 meV without other qualitative changes. Since the energy difference between the metastable state and the GS is small, it is expected that the monolayer CeI₂ could be easily tuned to a fully off-plane FM state with an external magnetic field. (~ 8.2 T for 0.94 meV).

VII. CONCLUSIONS

In this work, the ab-initio DFT+U calculations combined with OMC are performed to investigate the magnetic GS of monolayer CeI₂. The FM GS and FM metastable states are identified. It is shown that the metastable states have different magnetic properties with the magnetic GS. Thus, we recommend that something ought to be done to prevent the metastable states from producing errors when predicting the magnetic properties of such local-electron systems by DFT calculations. The T_C of monolayer CeI₂ is simulated to be about 128 K based on the magnetic ground state, not above room temperature as mentioned before. The calculations of on-site $d-f$ exchange parameter and $4f$ electronic orbital energy point out that the GS of monolayer CeI₂ with FM order requires the harmony of both $4f$ and $5d$ electronic states to minimize the total energy. With SOC included, the easy axis of magnetization is found to be coupled with the crystal structure. The FM GS with both in-

plane and off-plane components of magnetic moments, and a fully off-plane FM metastable state of monolayer CeI₂ are confirmed to be close in total energy. Our work shows it is necessary to absorb SOC into the energy functional to allow SOC to affect the electronic state of the local electrons during the self-consistence calculations. Only in this way could the reliable magnetic GS of monolayer CeI₂ be obtained and the magnetic anisotropy be reliably described.

For other systems with local-electron magnetism, the identification of the local electronic states are also significant. However, the phenomenon of trapping into metastable states during the calculations is quite common and it causes confusions if no extra information is given. Here it is recommended to give the specific representation of the calculated local electronic state in one's research. This action helps to enhance the repeatability and normalization of the computational studies for magnetic materials. (All the representations of the used starting points and corresponding final states in our work have been shown in Section G of the Supporting information.)

Acknowledgments

This work was supported by the National Natural Science Foundation of China (Grant No. 12175023).

-
- [1] N. D. Mermin and H. Wagner, *Phys. Rev. Lett.* **17**, 1133 (1966).
 - [2] X. Jiang, Q. Liu, J. Xing, N. Liu, Y. Guo, Z. Liu, and J. Zhao, *Appl. Phys. Rev.* **8**, 031305 (2021).
 - [3] B. Huang, G. Clark, E. Navarro-Moratalla, D. R. Klein, R. Cheng, K. L. Seyler, D. Zhong, E. Schmidgall, M. A. McGuire, D. H. Cobden, W. Yao, D. Xiao, P. Jarillo-Herrero, and X. Xu, *Nature* **546**, 270 (2017).
 - [4] S. Tian, J.-F. Zhang, C. Li, T. Ying, S. Li, X. Zhang, K. Liu, and H. Lei, *J. Am. Chem. Soc.* **141**, 5326 (2019).
 - [5] X. Cai, T. Song, N. P. Wilson, G. Clark, M. He, X. Zhang, T. Taniguchi, K. Watanabe, W. Yao, D. Xiao, M. A. McGuire, D. H. Cobden, and X. Xu, *Nano Lett.* **19**, 3993 (2019).

- [6] Z. Zhang, J. Shang, C. Jiang, A. Rasmita, W. Gao, and T. Yu, *Nano Lett.* **19**, 3138 (2019).
- [7] A. Banerjee, J. Yan, J. Knolle, C. A. Bridges, M. B. Stone, M. D. Lumsden, D. G. Mandrus, D. A. Tennant, R. Moessner, and S. E. Nagler, *Science* **356**, 1055 (2017).
- [8] B. Zhou, Y. Wang, G. B. Osterhoudt, P. Lampen-Kelley, D. Mandrus, R. He, K. S. Burch, and E. A. Henriksen, *J. Phys. Chem. Solids* **128**, 291 (2019).
- [9] M. Bonilla, S. Kolekar, Y. Ma, H. C. Diaz, V. Kalappattil, R. Das, T. Eggers, H. R. Gutierrez, M.-H. Phan, and M. Batzill, *Nature Nanotechnol.* **13**, 289 (2018).
- [10] J. Li, B. Zhao, P. Chen, R. Wu, B. Li, Q. Xia, G. Guo, J. Luo, K. Zang, Z. Zhang, H. Ma, G. Sun, X. Duan, and X. Duan, *Adv. Mater.* **30**, 1801043 (2018).
- [11] D. J. O’Hara, T. Zhu, A. H. Trout, A. S. Ahmed, Y. K. Luo, C. H. Lee, M. R. Brenner, S. Rajan, J. A. Gupta, D. W. McComb, and R. K. Kawakami, *Nano Lett.* **18**, 3125 (2018).
- [12] C. Gong, L. Li, Z. Li, H. Ji, A. Stern, Y. Xia, T. Cao, W. Bao, C. Wang, Y. Wang, Z. Q. Qiu, R. J. Cava, S. G. Louie, J. Xia, and X. Zhang, *Nature* **546**, 265 (2017).
- [13] X. Wang, K. Du, Y. Y. F. Liu, P. Hu, J. Zhang, Q. Zhang, M. H. S. Owen, X. Lu, C. K. Gan, P. Sengupta, C. Kloc, and Q. Xiong, *2D Mater.* **3**, 031009 (2016).
- [14] K. Kim, S. Y. Lim, J. Kim, J.-U. Lee, S. Lee, P. Kim, K. Park, S. Son, C.-H. Park, J.-G. Park, and H. Cheong, *2D Mater.* **6**, 041001 (2019).
- [15] G. Le Flem, R. Brec, G. Ouvard, A. Louisy, and P. Segransan, *J. Phys. Chem. Solids* **43**, 455 (1982).
- [16] Z. Fei, B. Huang, P. Malinowski, W. Wang, T. Song, J. Sanchez, W. Yao, D. Xiao, X. Zhu, A. F. May, W. Wu, D. H. Cobden, J. H. Chu, and X. Xu, *Nat. Mater.* **17**, 778 (2018).
- [17] A. F. May, D. Ovchinnikov, Q. Zheng, R. Hermann, S. Calder, B. Huang, Z. Fei, Y. Liu, X. Xu, and M. A. McGuire, *ACS Nano* **13**, 4436 (2019).
- [18] J.-U. Lee, S. Lee, J. H. Ryoo, S. Kang, T. Y. Kim, P. Kim, C.-H. Park, J.-G. Park, and H. Cheong, *Nano Lett.* **16**, 7433 (2016).
- [19] Y. Tian, M. J. Gray, H. Ji, R. J. Cava, and K. S. Burch, *2D Mater.* **3**, 025035 (2016).
- [20] Y. Deng, Y. Yu, Y. Song, J. Zhang, N. Z. Wang, Z. Sun, Y. Yi, Y. Z. Wu, S. Wu, J. Zhu, J. Wang, X. H. Chen, and Y. Zhang, *Nature* **563**, 94 (2018).
- [21] W. Liu, Y. Xu, S. Hassan, J. Weaver, and G. van der Laan, in *Handbook of Spintronics*, edited by Y. Xu, D. D. Awschalom, and J. Nitta (Springer, Dordrecht, Netherlands, 2016), pp. 709–756.

- [22] G. van der Laan, Phys. Rev. Lett. **82**, 640 (1999).
- [23] S. Sarikurt, Y. Kadioglu, F. Ersan, E. Vatansever, O. U. Akturk, Y. Yuksel, U. Akinci, and E. Akturk, Phys. Chem. Chem. Phys. **20**, 997 (2018).
- [24] H.-S. Kim and H.-Y. Kee, Phys. Rev. B **93**, 155143 (2016).
- [25] L. J. Sandilands, Y. Tian, K. W. Plumb, Y.-J. Kim, and K. S. Burch, Phys. Rev. Lett. **114**, 147201 (2015).
- [26] F. Li, K. Tu, and Z. Chen, J. Phys. Chem. C **118**, 21264 (2014).
- [27] C. Ataca, H. Sahin, and S. Ciraci, J. Phys. Chem. C **116**, 8983 (2012).
- [28] W. Chen, J.-m. Zhang, Y.-z. Nie, Q.-l. Xia, and G.-h. Guo, J. Magn. Magn. Mater. **508**, 166878 (2020).
- [29] H.-R. Fuh, C.-R. Chang, Y.-K. Wang, R. F. L. Evans, R. W. Chantrell, and H.- T. Jeng, Sci. Rep. **6**, 32625 (2016).
- [30] H. Pan, J. Phys. Chem. C **118**, 13248 (2014).
- [31] M. Kan, S. Adhikari, and Q. Sun, Phys. Chem. Chem. Phys. **16**, 4990 (2014).
- [32] G. T. Lin, H. L. Zhuang, X. Luo, B. J. Liu, F. C. Chen, J. Yan, Y. Sun, J. Zhou, W. J. Lu, P. Tong, Z. G. Sheng, Z. Qu, W. H. Song, X. B. Zhu, and Y. P. Sun, Phys. Rev. B **95**, 245212 (2017).
- [33] M.-W. Lin, H. L. Zhuang, J. Yan, T. Z. Ward, A. A. Puretzky, C. M. Rouleau, Z. Gai, L. Liang, V. Meunier, B. G. Sumpter, P. Ganesh, P. R. C. Kent, D. B. Geohegan, D. G. Mandrus, and K. Xiao, J. Mater. Chem. C **4**, 315 (2016).
- [34] H. Wang, F. Fan, S. Zhu, and H. Wu, Europhys. Lett. **114**, 47001 (2016).
- [35] W.-B. Zhang, Q. Qu, P. Zhu, and C.-H. Lam, J. Mater. Chem. C **3**, 12457 (2015).
- [36] J. Liu, Q. Sun, Y. Kawazoe, and P. Jena, Phys. Chem. Chem. Phys. **18**, 8777 (2016).
- [37] W. Jiang, Y. Hou, S. Li, Z. Fu, and P. Zhang, Chinese Phys. B **30**, 127501 (2021).
- [38] A. I. Liechtenstein, V. V. Anisimov, J. Zaanen, Phys. Rev. B **52**, R5467 (1995).
- [39] S. L. Dudarev, G. A. Botton, S. Y. Savrasov, C. J. Humphreys and A. P. Sutton, Phys. Rev. B **57**, 1505 (1998).
- [40] Jeremy P. Allen and Graeme W. Watson, Phys. Chem. Chem. Phys. **16**, 21016-21031 (2016).
- [41] A. B. Shick, W. E. Pickett, and A. I. Liechtenstein, Journal of Electron Spectroscopy and Related Phenomena **114–116**, 753-758 (2001).
- [42] A. Miskowiec, Phys. Chem. Chem. Phys. **20**, 10384-10395 (2018).

- [43] B. Dorado, B. Amadon, M. Freyss, and M. Bertolus, *Phys. Rev. B* **79**, 235125 (2009).
- [44] B. Dorado, G. Jomard, M. Freyss, and M. Bertolus, *Phys. Rev. B* **82**, 035114 (2010).
- [45] B. Dorado, M. Freyss, B. Amadon, M. Bertolus, G. Jomard and P. Garcia, *J. Phys.: Condens. Matter* **25**, 333201 (2013).
- [46] M. S. Christian, E. R. Johnson, and Theodore M. Besmann, *J. Phys. Chem. A* **125**, 2791-2799 (2021).
- [47] A. Claisse, M. Klipfel, N. Lindbom, M. Freyss, and P. Olsson, *Journal of Nuclear Materials* **478**, 119-124 (2016).
- [48] G. Jomard, B. Amadon, F. Bottin, and M. Torrent, *Phys. Rev. B* **78**, 075125 (2008).
- [49] Y. Hou, W. Jiang, S. Li, Z. Fu, and P. Zhang, *Chinese Phys. B* **32**, 027103 (2022).
- [50] F. Jollet, G. Jomard, and B. Amadon, *Phys. Rev. B* **80**, 235109 (2009).
- [51] L. E Ratcliff, L. Genovese, H. Park, P. B Littlewood and Alejandro Lopez-Bezanilla, *J. Phys.: Condens. Matter* **34**, 094003 (2022).
- [52] B. Meredig, A. Thompson, H. A. Hansen, and C. Wolverton, *Phys. Rev. B* **82**, 195128 (2010).
- [53] H. Y. Geng, Y. Chen, Y. Kaneta, M. Kinoshita, and Q. Wu, *Phys. Rev. B* **82**, 094106 (2010).
- [54] B. Amadon, F. Jollet, and M. Torrent, *Phys. Rev. B* **77**, 155104 (2008).
- [55] F. Zhou and V. Ozolins, *Phys. Rev. B* **83**, 085106 (2011).
- [56] S. Zhou, H. Ma, E. Xiao, K. Gofryk, C. Jiang, M. E. Manley, D. H. Hurley, and C. A. Marianetti, *Phys. Rev. B* **106**, 125134 (2022).
- [57] B. Amadon, *J. Phys.: Condens. Matter* **24**, 075604 (2012).
- [58] J. Rabone, and M. Krack, *Computational Materials Science* **71**, 157–164 (2013).
- [59] K. Sheng, Q. Chen, H. Yuan, and Z. Wang, *Phys. Rev. B* **105**, 075304 (2022).
- [60] Kresse G. and Furthmuller J., *Phys. Rev. B* **54**, 11169 (1996).
- [61] Blöchl P. E., *Phys. Rev. B* **50**, 17953 (1994).
- [62] Kresse G., Joubert D., *Phys. Rev. B* **59**, 1758 (1999).
- [63] Blöchl P. E., Först C. J., and Schimpl J. B., *Bull. Mater. Sci.* **26**, 33 (2003).
- [64] Perdew J. P., Burke K., and Wang Y., *Phys. Rev. B* **54**, 16533 (1996).
- [65] P. Larson, W. R. L. Lambrecht, A. Chantis, and M. van Schilfgaarde, *Phys. Rev. B* **75**, 045114 (2007).
- [66] A. A. Mostofi, J. R. Yates, Y. Lee, I. Souza, D. Vanderbilt, N. Marzari, *Computer Physics Communications* **178**, 685–699 (2008).

- [67] X. He, N. Helbig, M. J. Verstraete, and E. Bousquet, *Computer Physics Communications* **264**, 107938 (2021).
- [68] Y. Miyatake, M. Yamamoto, J. J. Kim, M. Toyonaga and O. Nagai, *J. Phys. C: Solid State Phys.* **19**, 2539 (1986).
- [69] K. Momma and F. Izumi, *J. Appl. Cryst.* **41**, 653-658 (2008).
- [70] V. Wang, N. Xu, J. Liu, G. Tang, and W. Geng, *Computer Physics Communications* **267**, 108033 (2021).
- [71] B. Wang, X. Zhang, Y. Zhang, S. Yuan, Y. Guo, S. Dong and J. Wang, *Mater. Horiz.* **7**, 1623-1630 (2020).
- [72] E. F. Worden, R. W. Solarz, and J. A. Paisner, *J. Opt. Soc. Am.* **68** (1978).